Bulletin of the Seismological Society of America, Vol. 107, No. 1, pp. –, February 2017, doi: 10.1785/0120160080

Fault Model for the 2015 Leucas (Aegean Arc) Earthquake: Analysis Based on Seismological and Geodetic Observations

by Vasso Saltogianni, Tuncay Taymaz, Seda Yolsal-Çevikbilen, Tuna Eken, Fanis Moschas, and Stathis Stiros

Abstract The 17 November 2015 M_w 6.6 earthquake in Leucas (Leukas, Lefkas, or Lefkada) Island in the Ionian Sea, western Aegean arc, was modeled using teleseismic long-period *P* and *SH* waveforms and Global Positioning System (GPS) slip vectors. Detailed fault modeling in this region, characterized by intense seismicity and deformation rates, usually assigned to the Cephalonia Transform fault, is a challenge because of the unfavorable observation system. To overcome this problem, we independently analyzed seismological and geodetic data and then jointly evaluated the results. The adopted model indicates that the 2015 earthquake can be assigned to a shallow strike-slip fault, with a minor component of thrusting, along the southwest coasts of Leucas and with relatively high slip for the area. Additionally, mostly low-angle fault solutions satisfying geodetic observations were identified but were not further investigated. The preferred fault model permits recognition that recent $M_w > 6.0$ earthquakes in the area, some marked by extreme peak ground accelerations, are associated with a string of strike slip (or oblique slip), occasionally overlapping fault segments with variable characteristics, along or close to the west coasts of Leucas and Cephalonia (Keffalinia, Kefalonia) Islands, whereas the catastrophic 1953 M_w 7.2 Cephalonia and other previous major earthquakes were associated with thrust faulting.

Electronic Supplement: Table of the Global Positioning System (GPS)-derived displacements and figures of *P*-wave first-motion polarities, comparison of earthquake source parameters, GPS time series, 2D projections of geodetic solutions, the variance–covariance matrix of the geodetic solution, and the geodetic variable slip model.

Introduction

On 17 November 2015, a magnitude M_w 6.6 earthquake occurred in Leucas (Leukas, Lefkas, or Lefkada) Island, in the Ionian Sea, at the west edge of the Aegean arc (Fig. 1); this is the most seismically active part of Greece and among the most seismically active regions in the world. Seismological evidence based on near-field data indicates that the 2015 Leucas earthquake was associated with a strike-slip fault southwest of the Island, filling a gap between recently activated faults (Sokos *et al.*, 2016) during the 2003 M_w 6.3 Leucas earthquake to the north (Benetatos *et al.*, 2005; Zahradník *et al.*, 2005; Saltogianni and Stiros, 2015) and during the 2014 M_w 6.0 earthquakes in western Cephalonia (Keffalinia or Kefalonia) to the south (Merryman Boncori *et al.*, 2015; Sokos *et al.*, 2015; Fig. 1a). The detailed study of this earthquake is important for three main reasons.

First, modeling of earthquakes in the Ionian region is a challenge. This is mainly due to the geography of the area, leading to uneven distribution of seismological and geodetic observations (Fig. 1), and hence to observation systems with high degrees of freedom, and thus to unstable and not well-constrained solutions. An example illustrating this problem is that the second main event, M_w 6.0 of the 2014 Cephalonia sequence (2014b in Fig. 1), could not be fully constrained by seismological data (Sokos *et al.*, 2015).

Second, the 2015 Leucas earthquake is important to understand the relationship between recent earthquakes, the structural fabric of western Greece (the area west of the Pindus thrust in Fig. 1b), and its high deformation rates (Hollenstein *et al.*, 2008; Floyd *et al.*, 2010; Mouslopoulou *et al.*, 2014). This triple relationship is, however, not clear. Western Greece is dominated by imbricate east-dipping thrusts, some hundreds of kilometers long (Mercier *et al.*, 1979; Bornovas and Rondoyanni, 1983; Underhill, 1989). Many of these thrusts are active, as is inferred from coastal uplifts (Pirazzoli *et al.*, 1996) and seismicity (Louvari *et al.*, 1999; Shaw and Jackson, 2010). The most striking example is the highly

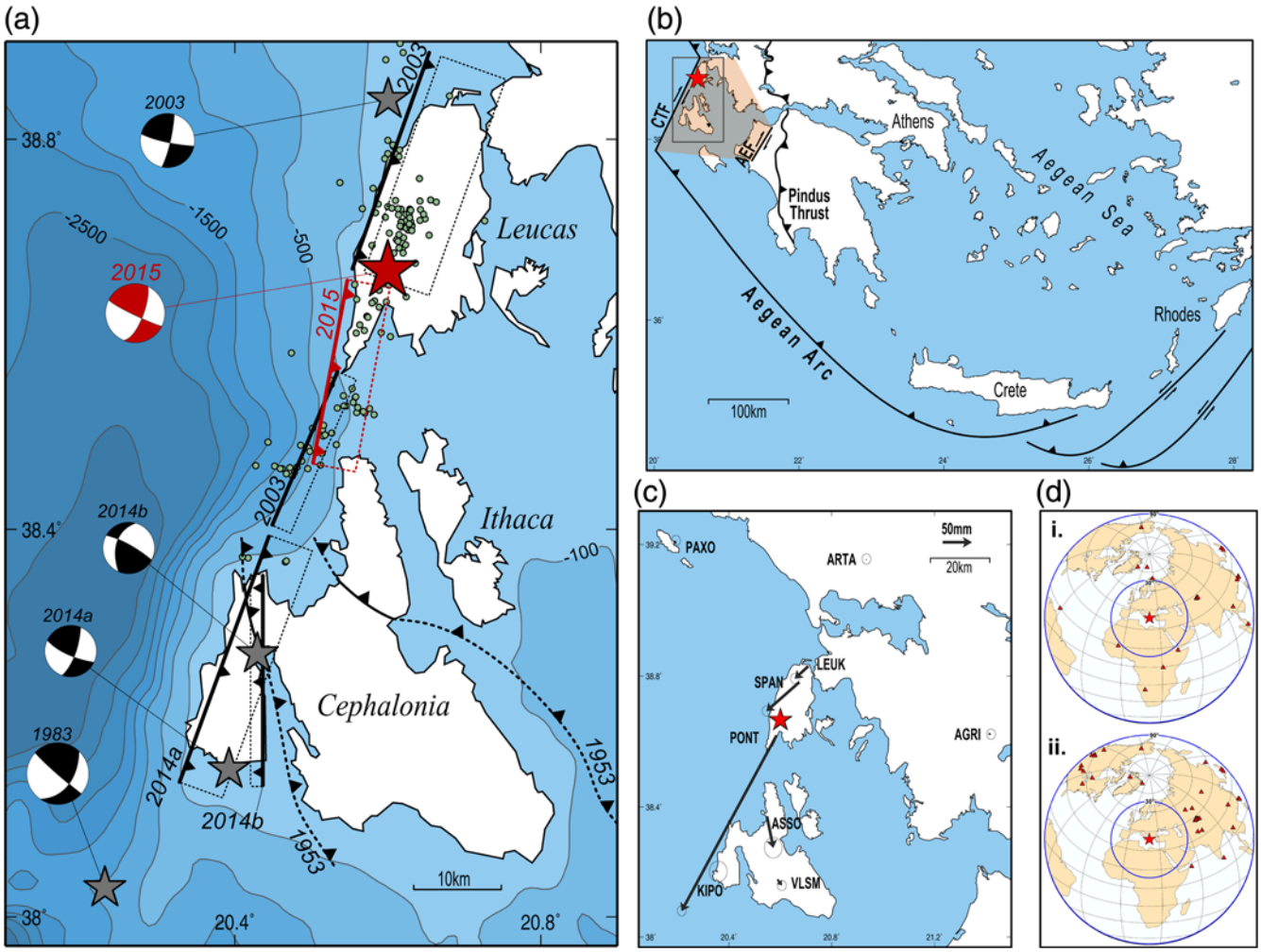

Figure 1. (a) The 2015 Leucas earthquake in relation to recent earthquakes (stars) in the area, along with the aftershock activity ($M_L > 3.0$, small circles) during the first 15 days after the mainshock. The 2015 event fills a gap in recent faulting since the 2003 earthquake (after Zahradník *et al.*, 2005; Saltogianni and Stiros, 2015). The two main faults of the 2014 Cephalonia sequence (after Merryman Boncori *et al.*, 2015; Sokos *et al.*, 2015), the 1953 thrusts (after Stiros *et al.*, 1994), and the 1983 earthquake data (after Kiratzi and Langston, 1991) are also shown. (b) The Aegean arc with inset indicating location map for (a). The 2015 earthquake (epicenter indicated by star) is located inside a shear zone (shaded area) between the Cephalonia Transform fault (CTF) to the west and the 2008 Achaia-Elia fault (AEF) to the east. Pindus thrust marks the east limit of a zone of east-dipping thrusts. (c) Global Positioning System (GPS) stations and horizontal coseismic slip vectors with 1σ error ellipses analyzed in this study. (d) Distribution of (i) teleseismic long-period seismic stations used in the point-source *P*- and *SH*-waveforms inversion, and (ii) of teleseismic broadband seismic stations used in finite-fault-slip inversion. Star and triangles denote earthquake location and seismic stations, respectively. The 30° and 90° epicentral distances are shown. The color version of this figure is available only in the electronic edition.

destructive 1953 Cephalonia M_w 7.2 earthquake, which produced 0.3–0.9 m uplift of the central part of Cephalonia (Fig. 1a; Stiros *et al.*, 1994). However, in more recent years, for which more detailed data exist, the release of seismic energy in the Ionian Islands was in several cases associated with segments of strike-slip or oblique-slip faults offshore Leucas and Cephalonia (Fig. 1a). This faulting is usually associated with the Cephalonia Transform fault (CTF), first reported after the 1983 M_w 7.0 earthquake (Fig. 1a; Scordilis *et al.*, 1985; Kiratzi and Langston, 1991; Louvari *et al.*, 1999; Sachpazi *et al.*, 2000; Yolsal-Çevikbilen and Taymaz, 2012). However, especially the faults of the 2014 Cephalonia earthquakes, usually assigned to the CTF, seem to cross Cephalonia (Fig. 1a; Sokos *et al.*, 2015), whereas the overall structure of CTF is not clear; a shear zone along the western part of the arc (Fig. 1b) is more likely (Saltogianni and Stiros, 2015; Sokos *et al.*, 2015).

Third, the Ionian Sea earthquakes are frequently associated with extreme peak ground accelerations (PGA), among the highest ever recorded in global scale (maximum value $0.77g$ for the 2014 Cephalonia earthquakes; Theodoulidis *et al.*, 2016). Finite modeling of reactivated faults is hence important to further study the PGA attenuation laws and their engineering implications.

In view of the difficulties for the modeling of earthquakes in the study area noticed above, we adopted an

approach proposed for the analysis of the 2014 M_w 6.9 earthquake at the North Aegean trough, at the continuation of the North Anatolian fault (Saltogianni *et al.*, 2015). We independently analyzed teleseismic and geodetic data to compute point and finite-fault models of this earthquake; these results were then jointly evaluated to understand the 2014 earthquake rupture processes and the active tectonics in the broader area of the Ionian Sea.

Seismological Data and Analysis

The analysis was based on inversion of long-period *P* and *SH* waveforms derived from the Federation of Digital Seismograph Networks (FDSN) and Global Digital Seismograph Network (GDSN), as well as on finite-fault modeling of slip using teleseismic broadband *P* body-wave data. The latter were confined to an epicentral distance range of 30°–90° (Fig. 1d). We determined source mechanism parameters and slip distribution on the fault plane of the 2015 Leucas earthquake by comparing the shapes and amplitudes of *P* and *SH* waveforms with calculated (synthetic) waveforms. For this modeling, we adopted the epicenter determined by the National Observatory of Athens (NOA), latitude = 38.665° N, longitude = 20.60° E.

Point-Source Inversion

We used the MT5 algorithm for the body-waveform inversion (Zwick *et al.*, 1994) to acquire source mechanism parameters. Velocity responses were converted into displacement records by reconvolving them with the response of the old World-Wide Standardized Seismographic Network (WWSSN) 15–100 s long-period instruments. A simplified crustal velocity-depth model was used, adopting conventional values for *P*-wave velocity at 6.8 km/s, *S*-wave velocity at 3.9 km/s, and density equal to 2.9 g/cm^3. Before waveform inversion, all seismograms were weighted according to the azimuthal distribution of stations (Ⓔ Fig. S1, available in the electronic supplement to this article). No filtering was applied to the waveforms. Amplitudes were also adjusted for geometrical spreading and for attenuation using operator $t^* = 1$ s for *P* and $t^* = 4$ s for *SH* waves (Futterman, 1962).

We selected for our analysis 18 *P*- and 7 *SH*-teleseismic waveforms, which have good azimuthal distribution on the focal sphere (Fig. 1d-i). Figure 2 indicates the comparison between observed and synthetic waveforms and complexities in both the *P* and *SH* waveforms in both polarity and shape changes, while the Doppler effect (i.e., directivity effects) is clearly seen at nodal stations. More explicitly, for *P* waveforms at stations MAJO, NACB, TKM2, SSLB, AAK, KMNB, UCH, ULHL, and CHTO, emergent positive, compressional, polarities are observed; stations ATD and MBAR are associated with impulsive positive first motions; stations TSUM, KOWA, and FDF with impulsive negative, dilatational, polarities; whereas stations DAG, COLA, KBS, and

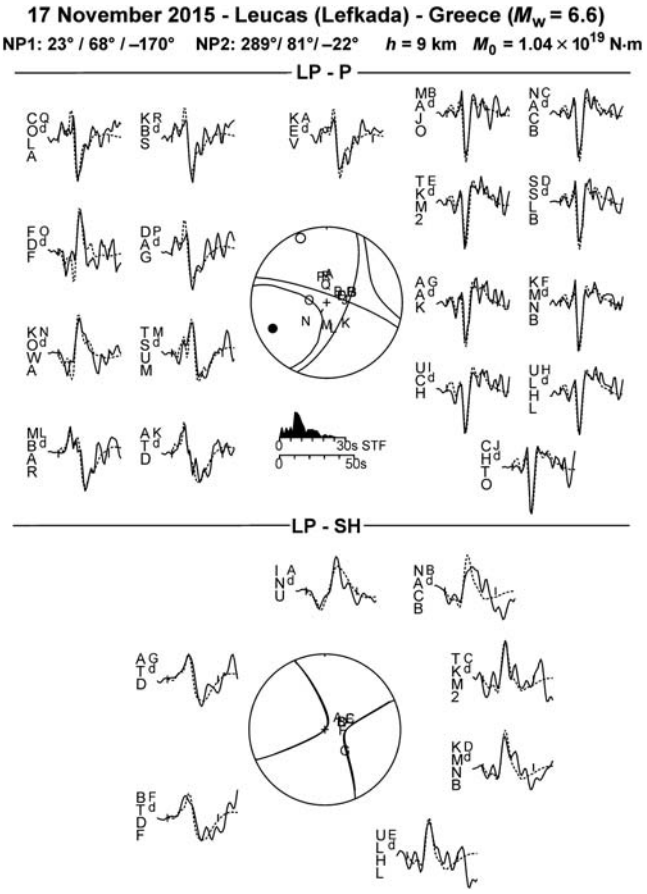

Figure 2. The radiation patterns and synthetic waveform fits for the adopted minimum misfit solution. Synthetic waveforms (dashed lines) fits to all long-period 18 *P*- and 7 *SH*-observed waveforms (solid lines) used in the inversion. The source time function (STF) and the time scale used for the waveforms are shown in the middle of the figure. Focal spheres are shown with *P* (top) and *SH* (bottom) nodal planes in lower hemisphere projections. *P* and *T* axes are marked by solid and open circles, respectively.

KEV with impulsive compressional polarities. Similar observations can be made at *SH* waveforms at stations INU, NACB, TKM2, KMNB, and ULHL with dilatational polarities, and BTDF and ATD with sharp compressional polarities (Fig. 2).

Inversion indicates an earthquake with right-lateral strike-slip faulting mechanism at a focal depth of 9 ± 2 km. The strike, dip, and rake angles of the fault plane is found to be 23° ± 5°, 68° ± 5°, and −170° ± 5°, respectively. We obtained a source time function (STF) representing the main moment release in about 25 s with a seismic moment value (M_0) of 1.04 × 10^{19} N·m (Fig. 2; Table 1). We applied many test runs, and based on those and by trial-and-error visual comparisons of waveforms of nodal station we could estimate uncertainties employing a widely used procedure proposed by McCaffrey and Nábělek (1987) and Molnar and Lyon-Cáen (1989). In this procedure, one simply fixes the source parameters at values close to those yielded by the minimum misfit solution, allowing all the others to vary

during the inversion. Then, the uncertainties are estimated by visual inspection of the deterioration level of the match between observed and synthetic seismograms. Formal standard deviations and variance values are too small to note. The minimum misfit following the inversion, described by the value of the minimum of the percent ratio of residual to data variance for phase data (R/D), is less than 20%. The best-fitting minimum misfit solution is also consistent with the distribution of *P*-wave first-motion polarities (Ⓔ Fig. S1).

In addition, we compared earthquake source parameters reported by Sokos *et al.* (2016) based on local/nearly local seismograms (at distances up to 80–200 km from the epicenter) and moment tensor catalogs (i.e., Global Centroid Moment Tensor [CMT], U.S. Geological Survey [USGS]-W phase) to our preferred minimum misfit double-couple point-source mechanism by selecting four *P* and four *SH* waveforms. The comparison of observed (solid lines) and synthetic seismograms (dashed lines) showed that the misfits obtained based on other source parameters are significantly larger than the one derived from the minimum misfit solution of this study. In Ⓔ Figure S2, it is clearly seen that our preferred point-source solution fits the waveforms well. We also tested the solution for alternative focal depths of 5 and 12 km. The corresponding waveform fits are apparently worse than those of the minimum misfit solution with a focal depth of 9 km (see Ⓔ Fig. S2).

Finite-Fault-Slip Inversion

We applied a new back-projection method that uses teleseismic *P* waveforms to integrate the direct *P* phase with reflected phases from structural discontinuities near the source (Yagi *et al.*, 2012) to determine the finite-fault-slip distribution model of the 2015 Leucas earthquake. It was assumed that faulting occurs on a single fault plane; strike and dip were obtained from the best-fitting point-source solution, whereas the slip (rake) angle varied during the whole rupture process. The theoretical Green's functions were calculated using the method of Kikuchi and Kanamori (1991) for the preliminary reference Earth velocity-depth model (Dziewonski and Anderson, 1981). Further details of the fault-slip distribution inversion can be found in Fielding *et al.* (2013) and Yolsal-Çevikbilen *et al.* (2014) and references therein.

A set of 35 teleseismic broadband *P* body-wave data series were retrieved from the FDSN–GDSN global network (Fig. 1d, part ii). The fault plane was divided into 13×6 subfaults with dimensions of 2×2 km^2. The STF (slip rate) of each subfault was expanded in a series of 19 overlapping triangle functions, each with a constant rise time of 1 s. The rupture front velocity was set as 3.2 km/s. The observed waveforms were then aligned on the basis of their first arrival time and converted into displacement waveforms with a sampling interval of 0.5 s. Furthermore, a Butterworth band-pass filter between 0.015 and 0.25 Hz has been applied to ease the effect of rupture process complexity for moderate-size earthquakes.

The preferred fault-slip model demonstrates that the slip occurs at the centroid with an area of maximum slip (~140 cm), indicating that rupture propagated mainly along the strike direction of the fault plane. STF reveals that the earthquake source duration was ~23 s. The size of the faulting area (length 26 km and width 12 km) is estimated to be ~312 km^2 from the slip model by considering the effective slip area on the fault plane (see Fig. 3) and, using the seismic moment value of M_0 0.61×10^{19} N·m, we calculated the stress drop to be ~28 bars.

These values, however, are relatively small compared to the seismic moment value of M_0 1.04×10^{19} N·m obtained from double-couple single-source *P* and *SH* waveforms (see Fig. 3; Table 1).

Geodetic Data and Analysis

Data

In our analysis, we used Global Positioning System (GPS) data with 30 s sampling from seven permanent stations continuously recording during the day of the earthquake and covering near- and far-field effects. Data from an additional permanent station (KIPO) with gaps and from a survey station (ASSO) were also used (Fig. 1c).

Coordinates for each of the seven continuous stations were obtained using the precise point positioning (PPP) method (Zumberge *et al.*, 1997) and the Canadian Spatial Reference System-PPP (CSRS-PPP) online processing tool. Records of 15 hrs long, ~7.5 hrs before and after the earthquake, were analyzed. Such an interval of records is long enough to minimize the drift that may characterize CSRS-PPP solutions (Moschas *et al.*, 2014).

The time series of coordinates indicate significant coseismic displacements, with a maximum of ~35 cm at PONT, proximal to the epicenter (Fig. 1c). The signature of a magnitude 5.0 aftershock, ~85 min after the mainshock, is also evident in the time series of station PONT (Ⓔ Fig. S3). For this reason and to be confined to displacements related to the mainshock, coseismic displacements were obtained from the difference between trend lines best fitting to time series of preseismic coordinates about 7.5 hrs long and of postseismic coordinates (just after the mainshock and before the major aftershock) 70 min long.

For stations KIPO and ASSO in Cephalonia Island, a different strategy was followed. Using the CSRS-PPP tool, we computed mean daily solutions bracketing intervals containing the earthquake (Ⓔ Fig. S4). The velocity of station ASSO was approximated by a velocity field computed through kriging from stations shown in Ⓔ Figure S5 and for which there were available observations covering an interval of ~3 years. Then, we extrapolated the available preseismic coordinates in each station/axis forward and the postseismic coordinates backward until the day of the earthquake, and from their difference we computed coseismic displacements.

Coseismic displacements for all stations are summarized in Ⓔ Table S1. Their uncertainties were estimated based on the errors derived from the linear regressions applying the

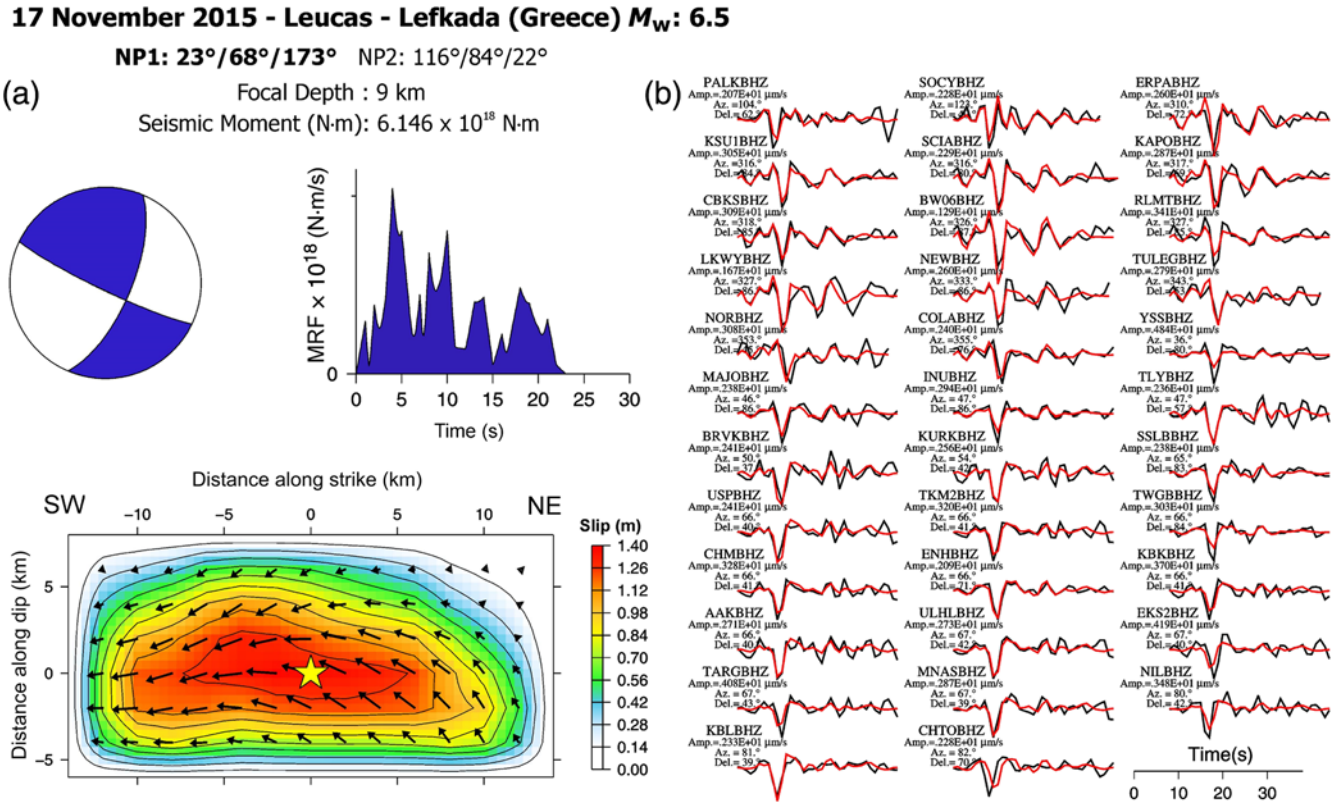

Figure 3. (a) Focal mechanism, total moment rate function, and coseismic slip distribution (contour lines correspond to the scale interval at the right) of the 2015 Leucas earthquake derived from body-wave finite-fault inversion. Slip model is derived on NP1. A star indicates the location of the rupture initiation (initial break) located at a focal depth of about 9 km. The slip vectors and the distribution of slip magnitudes are also illustrated. (b) Comparison of the observed and synthetic broadband *P* waveforms used in slip distribution inversion. Station code, amplitude, station azimuth, and distances are given above waveforms. The color version of this figure is available only in the electronic edition.

law of error propagation (see Mikhail, 1976). However, fluctuations in computed uncertainties may be coincidental because the law of error propagation covers random errors only, whereas GPS data are affected by a combination of white and colored noise (Williams, 2003; Mouslopoulou *et al.*, 2014). In addition, solutions deriving from observations of a few hours despite their long-period noise, describe well relative displacements (such as seismic dislocations), though with different levels of short-period noise (Moschas *et al.*, 2014). For this reason, and because the inversion algorithm adopted is strongly based on weighting of observations (Saltogianni and Stiros, 2015), we adopted flat errors for each coordinate, roughly corresponding to the mean values of computed random error uncertainties (Ⓔ Table S1). For stations KIPO and ASSO, with lower quality of data, we adopted uncertainties double those corresponding to the other stations; these are realistic estimates based on our experience from other cases in the region.

Inversion Methodology

For the finite-fault modeling, we used the Okada (1985) formula for uniform slip faulting and the TOPological INVersion (TOPINV) algorithm (Saltogianni and Stiros, 2015), which has the following characteristics:

1. It permits simultaneous inversion of all n unknown variables through an exhaustive uniform search of hypergrid points (grid points in the R^n space) of a grid G, covering a selected search space. The analysis is based on an optimization parameter k, and the overall search is repeated until the optimal value of k is obtained.
2. It does not search among a small sample of possible solutions to identify a single point, which is characterized by minimum mean misfit between observations and model predictions (see Cervelli *et al.*, 2001; Sambridge and Mosegaard, 2002; Menke, 2012), but it identifies one or more compact clusters of points in the R^n space satisfying the observation equations. This is possible on the basis of transformation of observation equations into inequalities, functions of k and of the observation errors. Each cluster of grid points corresponds to a set of possible solutions, and the corresponding best stochastic solution and its variance–covariance matrix are computed using first and second statistical moments (see Mikhail, 1976).

To avoid any excessive computational load, which is common in exhaustive searching, the inversion is performed adopting nested grids; at first a coarse solution is identified in a wide and coarse grid (grid G1), and then finer solutions are obtained by forming essentially nested finer grids (grids G2, G3, etc.).

Table 1
Seismological and Geodetic Results for the 2015 Leucas Earthquake

	Seismological Modeling		Geodetic Uniform Slip Modeling			
	Single Point	Finite Fault	Search Grid G1 Range/Spacing	Preliminary (Coarse) Solution	Search Grid G2 Range/Spacing	Final (Refined) Solution
E (°) source	20.600*	20.600*	-	-	-	-
E (°) fault center	-	-	20.335–20.792/0.04	-	-	20.553
E (km) fault center	-	-	20–60/5	40	36–44/2	39 ± 1
N (°) source	38.665*	38.665*	-	-	-	-
N (°) fault center	-	-	38.977–38.739/0.04	-	-	38.561
N (km) fault center	-	-	30–70/5	50	47–53/2	50 ± 1
Source depth (km)	9 ± 2	-	-	-	-	-
Depth of upper tip (km)	-	-	0–5/1	0	0–1/0.2	0.2 ± 0.2
Strike (°)	23 ± 5	23*	0–40/5	10	6–14/2	10 ± 3
Dip (°)	68 ± 5	68*	10–90/5	70	66–74/2	68 ± 2
Rake (°)	−170 ± 5	173	160–230/5	170	166–176/2	173 ± 2
Length (km)	-	26	20–60/5	20	16–24/2	21 ± 2
Width (km)	-	12	5–20/5	15	11–19/2	13.5 ± 2.0
Average slip (cm)	-	-	50–200/5	140	135–145/2.5	140 ± 3
Max slip (cm)	-	140	-	-	-	250
Number of grid points	-	-	$\sim 1.2 \times 10^9$	1	$\sim 3 \times 10^6$	~170
χ^2_v				3.45		2.75
Stress drop (bars)	47	27				
M_0 ($\times 10^{19}$) (N·m)	1.0	0.6				1.2 ± 0.2
M_w	6.6	6.5				6.70 ± 0.05

Details of the input data and results of the seismological point-source and finite-fault models and of the uniform slip geodetic model.
*A *priori* input values in models.

The details of the inversion methodology are explained in Saltogianni and Stiros (2012, 2015), Saltogianni *et al.* (2014), and in the Ⓔ electronic supplement to this article.

Computations and Results

Using the coseismic displacements of Ⓔ Table S1, a system of 26 observation equations was formed with nine unknown variables that define the activated finite fault. These variables are the coordinates (easting and northing) of the center of the fault, the depth of its upper edge, the strike, dip, and rake angles, the length and width of the fault, and the amount of slip on the fault.

An additional condition (inequality) to discard physically unreasonable solutions (compare to Böse and Heaton, 2010) was added to exclude faults with unrealistic aspect ratios r (r = length/width, $r < 1.2$, $r > 4$). This led to a final system of 27 observation inequalities in the form of Ⓔ equation (S4).

To avoid any bias in our results, at first we adopted a very broad search space, much exceeding the margins of possible values defined by the available seismological estimates (e.g., Sokos *et al.*, 2016; this study). For example, dip and rake angles were allowed to range between 10°–90° and 160°–220°, respectively, to cover the possibility of both strike-slip and thrust faulting (compare to Louvari *et al.*, 1999; Shaw and Jackson, 2010). The details of grid G1 are shown in Table 1.

Values of k in decreasing order were tested, and an optimal value of $k = 3.05$ led to a set of 1322 grid points satisfying the observation system. These 9D points are shown in 2D projections in the $9(9 + 1)/2 = 36$ in total x–y plots of Figure 4. In these x–y plots, grid points do not correspond to one or more compact clusters but seem to have a diffuse pattern. However, the x–y plots for strike–dip and dip–rake indicate a discrete (isolated) solution (arrows in Fig. 4), corresponding to dip 70°, strike 10°, and rake 170°. This isolated point was regarded as a valid coarse (preliminary) solution within the resolution of the first-coarse grid G1, because (1) it is broadly consistent with the seismological estimates (Table 1), and (2) it corresponds to a small weighted mean misfit of $\chi^2_v = 3.45$.

Uniform Slip Fault Model

The coarse solution was further refined using a denser grid G2 around it that is consistent with modeling results from seismological data analysis. The margins of G2 were defined so that the spacing for each variable is 2.5 times smaller than in G1 and its width 1.6 times higher than the G1 spacing (see Table 1 and Fig. 4 and Ⓔ Fig. S6). Repeating the search for various values of k, a new refined solution was obtained for ~170 grid points, offering a mean misfit of $\chi^2_v = 2.75$. This refined solution is summarized in Table 1 and Ⓔ Figure S6 and corresponds to a strike-slip fault ~21 km long and ~13 km deep, with strike, dip, and rake angles at 10°, 68°, and 173°, respectively, with mean slip 140 cm and with seismic moment 1.2×10^{19} N·m (Fig. 5; Table 1).

The variance–covariance matrix of the refined solution is shown in Ⓔ Figure S7. Small covariances indicate that the solution is stable.

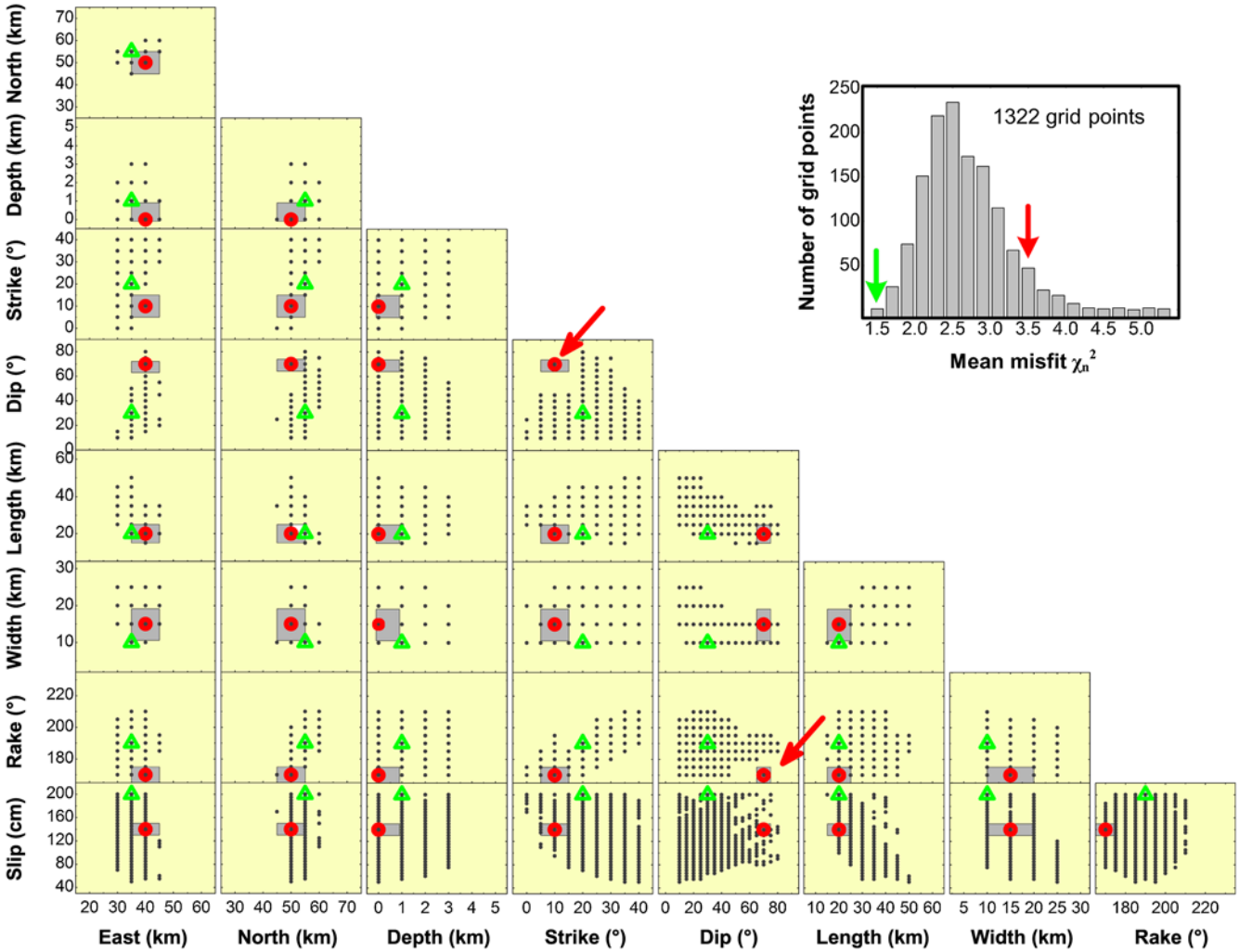

Figure 4. 2D projections of 1322 grid points (small dots) corresponding to the coarse (preliminary) solution for $k = 3.05$ in the limits of grid G1 (see Table 1). Apart from a rather diffuse set of points, in the panels of strike–dip and dip–rake a distinct solution (marked by arrows) is obvious, corresponding to strike 10°, dip 70°, and rake 170°. This solution clearly deviates from the other grid points and corresponds to mean misfit $\chi_v^2 = 3.45$. Shaded rectangles in each panel indicate grid G2 from which our preferred solution was derived (Table 1; Ⓔ Fig. S6, available in the electronic supplement to this article). The point (solution) of minimum misfit is marked in the panels with a triangle. The inset indicates the histogram of the mean misfit χ_v^2 of the 1322 grid points. Arrows point to the adopted coarse solution (right), not corresponding to the minimum misfit solution (left). The color version of this figure is available only in the electronic edition.

To further confirm its stability, we tested the impacts of dithering on the inversion. In each observation of Ⓔ Table S1, we added white noise with variance equal to the adopted uncertainties in observations. Using the new values of the variables as observations and grid G1, we applied the algorithm and found that for $k = 3.05$, the pattern of Figure 4 is fully reproduced (though with a smaller number of grid points, 754 instead of 1322) the same diffuse pattern of points and that the coarse (preliminary) solution is still clear; hence this solution seems to be stable.

Variable Slip Model

In addition to the uniform slip model, a variable slip model was computed using the SDM software (Wang *et al.*, 2012) and the refined solution. A homogeneous earth model, a fault-plane discretization patch of 2×2 km and a maximum slip of 3 m were assumed. Results shown in Ⓔ Figure S8 indicate maximum slip of 250 cm close to the center of the fault, attenuating to its edges, although this model is not corrected for zero slip at the fault edges. This pattern is qualitatively very similar to that derived from seismological data (Fig. 3).

Alternative Fault Models

The analysis of the grid G1 for $k = 3.05$ led to 1322 broadly distributed points in the R^9 space (Fig. 4), with each point representing solutions of the system of the observation equations from the mathematical point of view. Refinement of this search using smaller values of k was also tested for grid G1. For $k = 2.5$, a set of 14 grid points were recognized

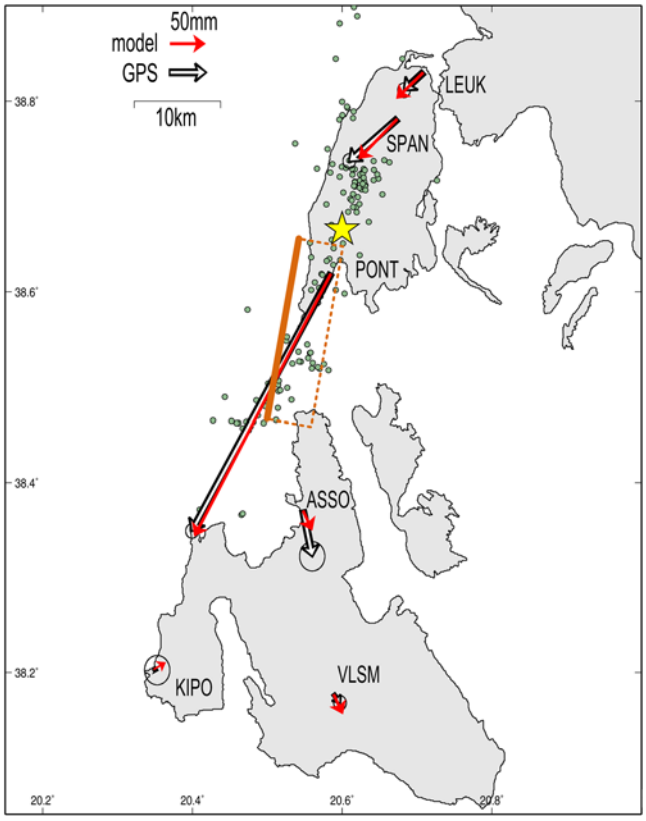

Figure 5. Observed (open arrows) and modeled (solid arrows) horizontal displacements at near-field stations (all displacement used in the modeling are shown in Fig. 1b and in Ⓔ Table S1). The surface trace of the modeled fault is indicated by a solid line and its horizontal (map) projection by a dashed rectangular. The epicenter (star) and main aftershocks (circles) of the 2015 Leucas earthquake are also shown (National Observatory of Athens database, see Data and Resources). The color version of this figure is available only in the electronic edition.

as potential solutions of the system of the equations. These 14 grid points, however, do not define compact spaces but potentially discrete, alternative models for the 2015 fault and different types of faulting, typically low dip (≤45°) faults (Ⓔ Fig. S9), and have not been further evaluated.

Clearly, such potential models could have been *a priori* discarded using narrow search spaces for specific variables, especially for dip angle, but this was not justified in a region characterized by active thrusting (see the Introduction).

Discussion

The difficulties in modeling seismic events in the west edge of the Aegean arc using regional and local seismological data due to the uneven geographic distribution of observation stations have been recently highlighted also by Sokos *et al.* (2015). A similar problem is expected with the global seismological stations used in this study (Fig. 1d). Geodetic stations analyzed are also unevenly distributed on one side of the fault, practically confined to the north and east part of it (Fig. 1c). Unfavorable distribution of observables (configuration defect in the network adjustment in the conventional geodetic nomenclature) tends to unstable, imprecise, or even to biased solutions. This was indeed reflected in our solutions. Because focal mechanisms indicate strike-slip and thrust faulting (Louvari *et al.*, 1999; Shaw and Jackson, 2010; Sokos *et al.*, 2016), we adopted a broad search space not *a priori* excluding any reasonable type of faulting. As a consequence, the adopted inversion algorithm for geodetic data identified different solutions (Fig. 4); this is because this algorithm is not oriented to one single minimum misfit solution, ignoring all others (see the Inversion of Geodetic Observations—The TOPINV Algorithm section in the Ⓔ electronic supplement to this article). Still, among them, one was clearly identified as a single discrete solution not corresponding to the minimum misfit (inset of Fig. 4). This solution was adopted because it was consistent with our seismological solution as well as with that proposed by Sokos *et al.* (2016). In addition, it was characterized by small uncertainties (Ⓔ Fig. S7) and was stable, as evident from its small covariances and sensitivity analysis based on dithering.

Model Assessment

The finite-fault model for the 2015 earthquake derived from our seismological and geodetic analyses corresponds to a shallow strike-slip fault offshore Leucas, most probably reaching the ground surface. This fault runs along the southwest coast of the Island, marked by high-gradient coastal relief and numerous landslides in easily erodible rocks, possibly masking faulting along the coast and seismic coastal uplifts, observed farther north (Pirazzoli *et al.*, 1994; Rondoyanni *et al.*, 2012).

Despite their overall consistency, there are some differences between the geodetic and the seismological model. The fault strike is estimated at $10° \pm 3°$ from geodetic data and $23° \pm 5°$ from seismological data (Table 1), but these two estimates are not different at the 95% probability level.

Also, the geodetic and seismological estimates of maximum slip differ by a factor of about 2 (Table 1). Because slip is the parameter with the maximum uncertainty even in cases with favorable distribution of observables (Cervelli *et al.*, 2001; Saltogianni and Stiros, 2015), this difference is reasonable. A high value of slip during the 2015 earthquake has also been reported by Chousianitis *et al.* (2016).

Finally, a difference in our estimations of seismic moment also exists, $1.2 \pm 0.2 \times 10^{19}$ N·m for the geodetic estimate, 1.04×10^{19} N·m for the seismological point-source inversion, and 0.61×10^{19} N·m for the seismological finite-fault modeling. However, these estimates are within the range derived by other methods and which differ by up to a factor of 3; 0.4×10^{19} N·m for NOA and 1.2×10^{19} N·m for GEOSCOPE (see Data and Resources). It is interesting to notice that estimates of seismic moment deriving from local and regional networks tend to show similar low values (NOA, and Sokos *et al.*, 2016; 0.6×10^{19} N·m), whereas global networks tend to show relatively larger values (GEOSCOPE and point-

source solution in this study), with the Global CMT solution in between (0.7×10^{19} N·m, see Data and Resources). Geodetic estimates of seismic moment also tend to show relatively high values; $1.2 \pm 0.2 \times 10^{19}$ N·m (this study) and $0.9–1.0 \times 10^{19}$ N·m (Ganas, Melgar, *et al.*, 2016, and Ganas, Elias, *et al.*, 2016), using GPS and Interferometric Synthetic Aperture Radar (InSAR) data.

Clearly, our geodetic estimate of seismic moment derives from simultaneous inversion for all fault parameters and computation of their uncertainties and from subsequent computation of the seismic moment from the formula

$$M_0 = \mu \times \text{Length} \times \text{Width} \times \text{Slip},$$

in which μ is the shear modulus of the rocks. Its uncertainty is computed applying the law of error propagation in its simplest form (Mikhail, 1976).

Such an estimate of seismic moment is expected to be more accurate than other estimates in which certain fault parameters are assumed *a priori* fixed (e.g., the epicenter), but they definitely contain errors that influence further calculations. Especially in unfavorable cases such as the Ionian Sea earthquakes, such errors may result in increased uncertainties and possibly biased estimations.

Despite that, we investigated three possible causes for the relatively high values in seismic moment derived from geodetic data.

The first cause is that geodetic data are contaminated by conventional postseismic displacements. This is not unreasonable for InSAR data, but GPS data analyzed in this study were derived from comparison of preseismic data (just before *P*-wave arrivals) and postseismic data covering an interval of 70 min after *P*-wave arrivals, during which no significant aftershocks occurred (see the Geodetic Data and Analysis section); hence no significant conventional coseismic displacements are likely.

The second cause is that computed displacements are sensitive to displacements related to seismic mobilization of evaporites, widespread in the area (Bornovas, 1964; BP Co. Ltd, 1971; Jackson and Talbot, 1986; Underhill, 1988; compare to Stiros *et al.*, 1994; Davison, 2009). Still, the impact of such motions can only be minor because mobilization of evaporites is expressed with much delay (Barnhart and Lohman, 2013; Nissen *et al.*, 2014) and because such mobilization is mostly expressed through vertical displacements. Vertical dislocations, however, were minimal in the 2015 earthquake, and, in addition, they can only weakly constrain the inversion model, because their weight is much smaller than that of horizontal, more precise, and larger amplitude displacements (Ⓔ Table S1).

The third cause is that the overall assumption was for elastic dislocation in a single uniform slip planar fault. Although the obtained misfit ($\chi^2_v < 4$; Fig. 5) indicates an excellent fit between observations and model predictions, local tectonics cannot exclude the possibility of a more complicated deformation pattern, perhaps including a combination of elastic and nonelastic deformation. Such scenarios may include (1) listric faulting, consistent with the pattern of thrust sheets dominating the area, (2) reduced friction along faults due to evaporitic intercalations (Bornovas, 1964) leading to increased surface slip values, or (3) a combination of faulting at depth (elastic deformation) and of anticline evolution (plastic deformation; see fig. 5 in Stiros *et al.*, 1994; see also Bornovas, 1964).

Tectonic and Seismological Implications

Our preferred fault model for the 2015 Leucas earthquake (Fig. 1; Table 1) indicates strike-slip (better, oblique slip) faulting along the west coasts of Leucas. The significance of the reactivated modeled fault can be derived from Figure 1, which summarizes existing evidence of faulting for all $M_w > 6$ earthquakes in the area since 1953. The 1953 fault pattern is derived from coastal uplifts (after Stiros *et al.*, 1994); the 1983 fault is defined by its focal mechanism (after Kiratzi and Langston, 1991); whereas finite faults are shown for the 2003 (Saltogianni and Stiros, 2015), 2014 (Merryman Boncori *et al.*, 2015; Sokos *et al.*, 2015), and 2015 (this study) earthquakes.

A first conclusion is that the 2003 and 2015 faults, despite their differences in geometric characteristics (like dip and strike angles), tend to represent segments of a major fault (or fault zone) and that the 2015 activated fault filled a gap between the two 2003 segments, as first noticed by Sokos *et al.* (2016). Still, a partial overlap between the 2015 fault and the south (Leucas segment) of the 2003 earthquake is likely. This overlap seems reliable, controlled by the slip vectors in Cephalonia (Fig. 1b), and is consistent with overlapping faults of the 2014 earthquakes in Cephalonia (Fig. 1a; Merryman Boncori *et al.*, 2015; Sokos *et al.*, 2015).

A likely explanation for the variability in the geometric characteristics of these faults is that the crust in the study area is highly fragmented and built by a system of imbricate thrusts with a nearly north-northwest trend (BP Co. Ltd, 1971; Mercier *et al.*, 1979; Underhill, 1989). For this reason, shear is not accommodated by a single continuous fault but by pre-existing planes of weakness in a broad shear zone (Fig. 1b); the west edge of this zone accommodates most of the deformation along a rather narrow strip of fault segments with different characteristics. Reactivation of fault segments with limited length tends to produce rather moderate magnitude earthquakes ($M_w < 7$), whereas the proximity of faults to inhabited areas is to some degree responsible for frequently observed extreme accelerations (PGA $\sim 0.5g$ in the 2003 earthquake, Gazetas *et al.*, 2006; PGA $0.77g$ in the 2014 earthquake, Theodoulidis *et al.*, 2016). The 2015 earthquake certainly produced much lower accelerations ($\sim 0.4g$; Earthquake Planning and Protection Organization [EPPO]-Institute of Engineering Seismology and Earthquake Engineering, see Data and Resources), but it was associated with slip several times higher than other previously activated faults (15–25 cm for the 2003 earthquake; Saltogianni and

Stiros, 2015). In addition, maximum slip was at the center of the fault and was attenuating toward its edges (Fig. 3 and Ⓔ Fig. S8), perhaps reflecting breaking of a strong asperity (Sokos *et al.*, 2016).

The 2015 fault model allows us to recognize that significant recent earthquakes in the area are associated with a string of strike-slip (or oblique-slip) faults along or close to the west coasts of Leucas and Cephalonia (usually assigned to the Cephalonia Transform fault, see Saltogianni and Stiros, 2015), whereas the 1953 and other previous major earthquakes were associated with thrust faulting farther east (Fig. 1a).

Conclusions

Independent inversion and combined evaluation of far-field and near-field data (teleseismic and GPS records, respectively) permitted us to overcome the limitations in the available data in the western part of the Aegean arc (mostly uneven distribution of observation stations) and to present a well-constrained finite-fault model for the 2015 earthquake. The latter seems to correspond to a shallow strike-slip fault with a minor component of thrusting along the Leucas coasts. Differences, especially in the strike, slip, and seismic moment, between seismological and geodetic estimates definitely exist, but they are within limits of the uncertainties, whereas certain characteristics of the faulting, such as the variable slip pattern, are very much consistent. Clearly, the analysis of geodetic data provided evidence of alternative low-angle faults, but this alternative was not further examined because of the seismological constraints.

The modeled fault seems to have filled a gap between the two faults reactivated in 2003, though with some overlap with one of them. This seems not to be a problem because the two faults of the Cephalonia 2014 earthquakes, also overlapping, are located in the same crustal volume (Fig. 1a; Sokos *et al.*, 2015). However, the spatiotemporal relationship between these moderate strike-slip earthquake events with major thrust-faulting earthquakes (e.g., the 1953 Cephalonia earthquake) remains unclear.

Data and Resources

P and *SH* waveforms were obtained by the Federation of Digital Seismograph Networks (FDSN) and the Global Digital Seismograph Network (GDSN) stations (Wilber-3 at http://ds.iris.edu/wilber3/find_event; last accessed November 2015). SAC2000 software (Goldstein *et al.*, 2003) was used to process conventional earthquake data (https://ds.iris.edu/ds/newsletter/vol10/no2/sac-software; last accessed November 2015). Global Positioning System (GPS) data come from the National Observatory of Athens (NOA) network (PONT, SPAN, VLSM, and KIPO; http://www.gein.noa.gr/services/GPS/noa_gps.html; last accessed March 2016), METRICA network (AGRI, ARTA, and PAXO), URANUS network (LEUK), and the Patras University network (ASSO). Their analysis was primarily based on the online processing tool Canadian Spatial Reference System-precise point positioning (CSRS-PPP) provided by Natural Resources Canada (http://www.nrcan.gc.ca/; last accessed January 2016). Epicenters and focal mechanisms plotted in Figures 1a and 5 were derived from the NOA database (http://bbnet.gein.noa.gr/HL/; last accessed January 2016; Kiratzi and Langston, 1991; Zahradník *et al.*, 2005; Sokos *et al.*, 2015). Reported focal mechanisms of the 2015 Leucas earthquake by NOA, GEOSCOPE Observatory, and Global Centroid Moment Tensor (CMT) are available at http://bbnet.gein.noa.gr/mt_solution/2015/151117_07_10_07.31_MTsol.html (last accessed August 2016), at http://geoscope.ipgp.fr/index.php/en/catalog/earthquake-description?seis=us10003ywp (last accessed August 2016), and at http://www.globalcmt.org/CMTsearch.html (last accessed August 2016), respectively. The preliminary report of the 2015 Leucas earthquake by EPPO-ITSAK is available at http://www.itsak.gr/uploads/news/earthquake_reports/Lefkas_M6.0_17-11-2015.pdf (last accessed August 2016). Some of the figures were produced using the Generic Mapping Tools (GMT) software available at http://gmt.soest.hawaii.edu/ (last accessed January 2016).

Acknowledgments

We are very grateful to Associate Editor Bill Hammond and three anonymous reviewers for their constructive comments that improved this article. We also thank A. Ganas (National Observatory of Athens [NOA]) for making available the Global Positioning System (GPS) records of stations AGRI, ARTA, and PAXO, and G. Polykretis (Tree Co) for those of station LEUK of the URANUS network. T. T. acknowledges support from the Turkish Academy of Sciences (TÜBA) in the framework for Young Scientist Award Program (TT-TÜBA-GEBİP 2001-2-17), İstanbul Technical University Research Fund (İTÜ-BAP), Turkish National Scientific, Technological Foundation (TÜBİTAK), and Alexander von Humboldt Foundation (AvH). We are grateful to Yuji Yagi for providing codes for finite-fault analysis and for his suggestions.

References

Barnhart, W. D., and R. B. Lohman (2013). Phantom earthquakes and triggered aseismic creep: Vertical partitioning of strain during earthquake sequences in Iran, *Geophys. Res. Lett.* **40,** no. 5, 819–823, doi: 10.1002/grl.50201.

Benetatos, C., A. Kiratzi, Z. Roumelioti, G. Stavrakakis, G. Drakatos, and I. Latoussakis (2005). The 14 August 2003 Lefkada Island (Greece) earthquake: Focal mechanisms of the mainshock and of the aftershock sequence, *J. Seismol.* **9,** no. 2, 171–190, doi: 10.1007/s10950-005-7092-1.

Bornovas, J. (1964). Geological study of Leukas Island, *Geol. Geophys. Res. IGSR* **10,** 1 (in Greek with extended abstract in French).

Bornovas, J., and T. Rondoyanni (1983). *Geological Map of Greece*, 1:500,000 scale, Institute of Geology and Mineral Exploration, Athens, Greece.

Böse, M., and T. H. Heaton (2010). Probabilistic prediction of rupture length, slip and seismic ground motions for an ongoing rupture: Implications for early warning for large earthquakes, *Geophys. J. Int.* **183,** no. 2, 1014–1030, doi: 10.1111/j.1365-246X.2010.04774.x.

BP Co. Ltd. (1971). *The Geological Results of Petroleum Exploration in Western Greece*, Publication No. 10, Institute of Geology and Subsurface Research, Athens, Greece.

Cervelli, P., M. H. Murray, P. Segall, Y. Aoki, and T. Kato (2001). Estimating source parameters from deformation data, with an application to the

March 1997 earthquake swarm off the Izu Peninsula, Japan, *J. Geophys. Res.* **106,** no. 6, 11,217–11,237, doi: 10.1029/2000JB900399.

Chousianitis, K., A. O. Konca, G.-A. Tselentis, G. A. Papadopoulos, and M. Gianniou (2016). Slip model of the 17 November 2015 $M_w = 6.5$ Lefkada earthquake from the joint inversion of geodetic and seismic data, *Geophys. Res. Lett.* **43,** no. 15, 7973–7981, doi: 10.1002/2016GL069764.

Davison, I. (2009). Faulting and fluid flow through salt, *J. Geol. Soc. London* **166,** 205–216.

Dziewonski, A. M., and D. L. Anderson (1981). Preliminary reference Earth model, *Phys. Earth Planet. In.* **25,** no. 4, 297–356, doi: 10.1016/0031-9201(81)90046-7.

Fielding, E. J., P. R. Lundgren, T. Taymaz, S. Yolsal-Çevikbilen, and S. E. Owen (2013). Fault-slip source models for the 2011 M 7.1 Van earthquake in Turkey from SAR interferometry, pixel offset tracking, GPS and seismic waveform analysis, *Seismol. Res. Lett.* **84,** no. 4, 579–593, doi: 10.1785/0220120164.

Floyd, M. A., H. Billiris, D. Paradissis, G. Veis, A. Avallone, P. Briole, S. McClusky, J. M. Nocquet, K. Palamartchouk, B. Parsons, *et al.* (2010). A new velocity field for Greece: Implications for the kinematics and dynamics of the Aegean, *J. Geophys. Res.* **115,** no. B10403, doi: 10.1029/2009JB007040.

Futterman, W. I. (1962). Dispersive body waves, *J. Geophys. Res.* **67,** 5279–5291.

Ganas, A., P. Elias, G. Bozionelos, G. Papathanassiou, A. Avallone, A. Papastergios, S. Valkaniotis, I. Parcharidis, and P. Briole (2016). Coseismic deformation, field observations and seismic fault of the 17 November 2015 M = 6.5, Lefkada Island, Greece earthquake, *Tectonophysics* **687,** 210–222, doi: 10.1016/j.tecto.2016.08.012.

Ganas, A., D. Melgar, P. Briole, G. Jianghui, G. Papathanassiou, G. Bozionelos, A. Avallone, S. Valkaniotis, E. Mendonidis, P. Argyrakis, *et al.* (2016). Coseismic deformation and slip model of the 17 November 2015 M = 6.5 earthquake, Lefkada Island, Greece, *Geophys. Res. Abstr.* **18,** EGU2016–12041.

Gazetas, G., P. Dakoulas, and I. Anastasopoulos (2006). Failure of harbor quaywalls in the Lefkada 14-8-2003 earthquake, in *Proc. of the 5th Hellenic Conference on Geotechnical and Geoenvironmental Engineering*, Xanthi, Greece, 31 May–2 June 2006, Vol. 2, 159–166, http://library.tee.gr/digital/m2134/m2134_gazetas.pdf (last accessed March 2015).

Goldstein, P., D. Dodge, M. Firpo, and L. Minner (2003). 85.5 SAC2000: Signal processing and analysis tools for seismologists and engineers, in *International Handbook of Earthquake and Engineering Seismology, Part B*, W. H. K. Lee, H. Kanamori, P. C. Jennings, and C. Kisslinger (Editors), Vol. 81, International Geophysics, 1613–1614, Academic Press, London, United Kingdom.

Hollenstein, Ch., M. D. Müller, A. Geiger, and H.-G. Kahle (2008). Crustal motion and deformation in Greece from a decade of GPS measurements, 1993–2003, *Tectonophysics* **449,** nos. 1/4, 17–40, doi: 10.1016/j.tecto.2007.12.006.

Jackson, M., and C. Talbot (1986). External shapes, strain rates, and dynamics of salt structures, *Geol. Soc. Am. Bull.* **97,** 305–323.

Kikuchi, M., and H. Kanamori (1991). Inversion of complex body waves—III, *Bull. Seismol. Soc. Am.* **81,** no. 6, 2335–2350.

Kiratzi, A. A., and C. A. Langston (1991). Moment tensor inversion of the 1983 January 17 Kefallinia event of Ionian Islands (Greece), *Geophys. J. Int.* **105,** no. 2, 529–535, doi: 10.1111/j.1365-246X.1991.tb06731.x.

Louvari, E., A. Kiratzi, and B. Papazachos (1999). The Cephalonia transform fault and its extension to western Lefkada Island (Greece), *Tectonophysics* **308,** nos. 1/2, 223–236, doi: 10.1016/S0040-1951(99)00078-5.

McCaffrey, R., and J. L. Nábelek (1987). Earthquakes, gravity, and the origin of the Bali basin: An example of a nascent continental fold-and-thrust belt, *J. Geophys. Res.* **92,** 441–460, doi: 10.1029/JB092iB01p00441.

Menke, W. (2012). *Geophysical Data Analysis: Discrete Inverse Theory (MATLAB Edition)*, Third Ed., Elsevier, Amsterdam, The Netherlands.

Mercier, J.-L., N. Delibassis, A. Gauthier, J. Jarrige, F. Lemeille, H. Philip, M. Sebrier, and D. Sorel (1979). La neotectonique de l'arc Egeen, *Rev. Geol. Dyn. Geogr. Phys.* **21,** no. 1, 67–92 (in French).

Merryman Boncori, J. P., I. Papoutsis, G. Pezzo, C. Tolomei, S. Atzori, A. Ganas, V. Karastathis, S. Salvi, C. Kontoes, and A. Antonioli (2015). The February 2014 Cephalonia earthquake (Greece): 3D deformation field and source modeling from multiple SAR techniques, *Seismol. Res. Lett.* **86,** no. 1, 124–137, doi: 10.1785/0220140126.

Mikhail, E. M. (1976). *Observations and Least Squares*, IEP-A Dun-Donnelley Publisher, New York, New York.

Molnar, P., and H. Lyon-Cáen (1989). Fault plane solutions of earthquakes and active tectonics of the Tibetan plateau and its margins, *Geophys. J. Int.* **99,** 123–153, doi: 10.1111/j.1365-246X.1989.tb02020.x.

Moschas, F., A. Avallone, V. Saltogianni, and S.C. Stiros (2014). Strong motion displacement waveforms using 10-Hz precise point positioning GPS: An assessment based on free oscillation experiments, *Earthq. Eng. Struct. Dynam.* **43,** no. 12, 1853–1866, doi: 10.1002/eqe.2426.

Mouslopoulou, V., V. Saltogianni, M. Gianniou, and S. Stiros (2014). Geodetic evidence for tectonic activity on the Strymon Fault System, northeast Greece, *Tectonophysics* **633,** 246–255, doi: 10.1016/j.tecto.2014.07.012.

Nissen, E., J. Jackson, S. Jahani, and M. Tatar (2014). Zagros "phantom earthquakes" reassessed—The interplay of seismicity and deep salt flow in the Simply Folded Belt?, *J. Geophys. Res.* **119,** no. 4, 3561–3583, doi: 10.1002/2013JB010796.

Okada, Y. (1985). Surface deformation due to shear and tensile faults in a half space, *Bull. Seismol. Soc. Am.* **75,** no. 4, 1135–1154.

Pirazzoli, P. A., J. Laborel, and S. C. Stiros (1996). Earthquake clustering in the Eastern Mediterranean during historical times, *J. Geophys. Res.* **101,** no. 3, 6083–6097, doi: 10.1029/95JB00914.

Pirazzoli, P. A., S. C. Stiros, J. Laborel, F. Laborel-Deguen, M. Arnold, S. Papageorgiou, and C. Morhange (1994). Late-Holocene shoreline changes related to palaeoseismic events in the Ionian Islands, Greece, *Holocene* **4,** no. 4, 397–405.

Rondoyanni, T., M. Sakellariou, J. Baskoutas, and N. Christodoulou (2012). Evaluation of active faulting and earthquake secondary effects in Lefkada Island, Ionian Sea, Greece: An overview, *Nat. Hazards* **61,** no. 2, 843–860, doi: 10.1007/s11069-011-0080-6.

Sachpazi, M., A. Hirn, C. Clément, F. Haslinger, M. Laigle, E. Kissling, P. Charvis, Y. Hello, J.-C. Lépine, M. Sapin, and J. Ansorge (2000). Western Hellenic subduction and Cephalonia transform: Local earthquakes and plate transport and strain, *Tectonophysics* **319,** no. 4, 301–319, doi: 10.1016/S0040-1951(99)00300-5.

Saltogianni, V., and S. Stiros (2012). Adjustment of highly non-linear redundant systems of equations using a numerical, topology-based approach, *J. Appl. Geophys.* **6,** nos. 3/4, 125–134, doi: 10.1515/jag-2012-0018.

Saltogianni, V., and S. Stiros (2015). A two-fault model of the 2003 Leucas (Aegean arc) earthquake based on topological inversion of GPS data, *Bull. Seismol. Soc. Am.* **105,** no. 5, 2510–2520, doi: 10.1785/0120140355.

Saltogianni, V., M. Gianniou, T. Taymaz, S. Yolsal-Çevikbilen, and S. Stiros (2015). Fault slip source models for the 2014 M_w 6.9 Samothraki-Gökçeada earthquake (North Aegean trough) combining geodetic and seismological observations, *J. Geophys. Res.* **120,** no. 12, 8610–8622, doi: 10.1002/2015JB012052.

Saltogianni, V., S. C. Stiros, A. V. Newman, K. Flanagan, and F. Moschas (2014). Time-space modeling of the dynamics of Santorini volcano (Greece) during the 2011–2012 unrest, *J. Geophys. Res.* **119,** no. 11, 8517–8537, doi: 10.1002/2014JB011409.

Sambridge, M., and K. Mosegaard (2002). Monte Carlo methods in geophysical inverse problems, *Rev. Geophys.* **40,** no. 3, 3-1–3-29, doi: 10.1029/2000RG000089.

Scordilis, E. M., G. F. Karakaisis, B. G. Karacostas, D. G. Panagiotopoulos, P. E. Comninakis, and B. C. Papazachos (1985). Evidence for transform faulting in the Ionian Sea: The Cephalonia island earthquake sequence of 1983, *Pure Appl. Geophys.* **123,** no. 3, 388–397, doi: 10.1007/BF00880738.

Shaw, B., and J. Jackson (2010). Earthquake mechanisms and active tectonics of the Hellenic subduction zone, *Geophys. J. Int.* **181,** no. 2, 966–984, doi: 10.1111/j.1365-246X.2010.04551.x.

Sokos, E., A. Kiratzi, F. Gallovič, J. Zahradník, A. Serpetsidaki, V. Plicka, J. Kostelecký, and G.-A. Tselentis (2015). Rupture process of the 2014 Cephalonia, Greece, earthquake doublet (M_w 6) as inferred from regional and local seismic data, *Tectonophysics* **656,** 131–141, doi: 10.1016/j.tecto.2015.06.013.

Sokos, E., J. Zahradník, F. Gallovič, A. Serpetsidaki, V. Plicka, and A. Kiratzi (2016). Asperity break after 12 years: The M_w 6.4 2015 Lefkada (Greece) earthquake, *Geophys. Res. Lett.* **43,** no. 12, 6137–6145, doi: 10.1002/2016GL069427.

Stiros, S. C., P. A. Pirazzoli, J. Laborel, and F. Laborel-Deguen (1994). The 1953 earthquake in Cephalonia (Western Hellenic arc): Coastal uplift and halotectonic faulting, *Geophys. J. Int.* **117,** no. 3, 834–849, doi: 10.1111/j.1365-246X.1994.tb02474.x.

Theodoulidis, N., C. Karakostas, V. Lekidis, K. Makra, B Margaris, K. Morfidis, Ch. Papaioannou, E. Rovithis, T. Salonikios, and A. Savvaidis (2016). The Cephalonia, Greece, January 26 (M 6.1) and February 3, 2014 (M 6.0) earthquakes: Near-fault ground motion and effects on soil and structures, *Bull. Earthq. Eng.* **14,** no. 1, 1–38, doi: 10.1007/s10518-015-9807-1.

Underhill, J. R. (1988). Triassic evaporites and Plio-Quaternary diapirism in western Greece, *J. Geol. Soc.* **145,** 269–282, doi: 10.1144/gsjgs.145.2.0269.

Underhill, J. R. (1989). Late Cenozoic deformation of the Hellenide foreland, western Greece, *Geol. Soc. Am. Bull.* **101,** no. 5, 613–634, doi: 10.1130/0016-7606(1989)101<0613:LCDOTH>2.3.CO;2.

Wang, R., S. Parolai, M. Ge, M. Jin, T. R. Walter, and J. Zschau (2012). The 2011 M_w 9.0 Tohoku earthquake: Comparison of GPS and strong-motion data, *Bull. Seismol. Soc. Am.* **103,** 1336–1347, doi: 10.1785/0120110264.

Williams, S. D. P. (2003). The effect of coloured noise on the uncertainties of rates estimated from geodetic time series, *J. Geodes.* **76,** nos. 9/10, 483–494, doi: 10.1007/s00190-002-0283-4.

Yagi, Y., A. Nakao, and A. Kasahara (2012). Smooth and rapid slip near the Japan trench during the 2011 Tohoku-oki earthquake revealed by a hybrid back-projection method, *Earth Planet. Sci. Lett.* **355,** 94–101, doi: 10.1016/j.epsl.2012.08.018.

Yolsal-Çevikbilen, S., and T. Taymaz (2012). Earthquake source parameters along the Hellenic subduction zone and numerical simulations of historical tsunamis in the Eastern Mediterranean, *Tectonophysics* **536/537,** 61–100, doi: 10.1016/j.tecto.2012.02.019.

Yolsal-Çevikbilen, S., T. Taymaz, and C. Helvacı (2014). Earthquake mechanisms in the Gulfs of Gökova, Sığacık, Kuşadası, and the Simav Region (western Turkey): Neotectonics, seismotectonics and geodynamic implications, *Tectonophysics* **635,** 100–124, doi: 10.1016/j.tecto.2014.05.001.

Zahradník, J., A. Serpetsidaki, E. Sokos, and G.-A. Tselentis (2005). Iterative deconvolution of regional waveforms and a double-event interpretation of the 2003 Lefkada earthquake, Greece, *Bull. Seismol. Soc. Am.* **95,** no. 1, 159–172.

Zumberge, J. F., M. B. Heflin, D. C. Jefferson, M. M. Watkins, and F. H. Webb (1997). Precise point positioning for the efficient and robust analysis of GPS data from large networks, *J. Geophys. Res.* **102,** no. B3, 5005–5017, doi: 10.1029/96JB03860.

Zwick, P., R. McCaffrey, and G. Abers (1994). *MT5 Program, in Bibliographic References and BSSA Database (August, 1994)*, Vol. 4, IASPEI Software Library, http://www.iaspei.org/ (last accessed January 2016).

Department of Civil Engineering
University of Patras
Patras 26500, Greece
vsalt@upatras.gr
fmoschas@upatras.gr
stiros@upatras.gr
(V.S., F.M., S.S.)

The Faculty of Mines Department of Geophysical Engineering
Istanbul Technical University
Istanbul, Turkey
taymaz@itu.edu.tr
yolsalse@itu.edu.tr
eken@itu.edu.tr
(T.T., S.Y.-Ç., T.E.)

Manuscript received 10 March 2016;
Published Online 20 December 2016